

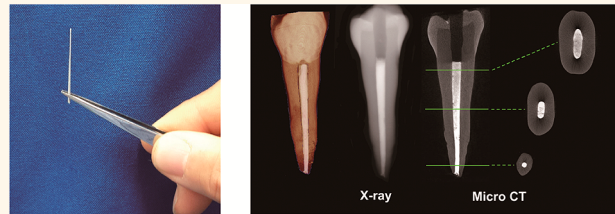


# Nanodiamond–Gutta Percha Composite Biomaterials for Root Canal Therapy

Dong-Keun Lee,<sup>\*,†</sup> Sue Vin Kim,<sup>†</sup> Adelheid Nerisa Limansubroto,<sup>†</sup> Albert Yen,<sup>‡</sup> Akrivoula Soundia,<sup>§</sup> Cun-Yu Wang,<sup>†,‡,||</sup> Wenyuan Shi,<sup>†,||</sup> Christine Hong,<sup>†</sup> Sotirios Tetradiis,<sup>§</sup> Yong Kim,<sup>||,§,¶,□</sup> No-Hee Park,<sup>||,§,◇</sup> Mo K. Kang,<sup>||,○</sup> and Dean Ho<sup>\*,†,‡,||,△,▽,○</sup>

<sup>†</sup>Division of Oral Biology and Medicine, <sup>§</sup>Division of Diagnostic and Surgical Sciences-Section of Oral and Maxillofacial Radiology, <sup>‡</sup>Division of Growth & Development-Section of Orthodontics, <sup>#</sup>Laboratory of Stem Cell & Cancer Epigenetic Research, <sup>¶</sup>Center for Oral and Head/Neck Oncology Research Center, Division of Oral Biology & Medicine, <sup>○</sup>Division of Constitutive and Regenerative Sciences-Section of Endodontics, <sup>△</sup>Division of Advanced Prosthodontics, <sup>▽</sup>The Jane and Jerry Weintraub Center for Reconstructive Biotechnology, and <sup>◇</sup>Laboratory Viral Oncology and Aging Research, UCLA School of Dentistry, Los Angeles, California 90095, United States, <sup>||</sup>Department of Bioengineering, UCLA Henry Samueli School of Engineering and Applied Science, Los Angeles, California 90095, United States, <sup>||</sup>Jonsson Comprehensive Cancer Center and <sup>○</sup>California NanoSystems Institute, UCLA, Los Angeles, California 90095, United States, <sup>□</sup>UCLA Broad Stem Cell Research Center, Box 957357, Los Angeles, California 90095, United States, and <sup>○</sup>Department of Medicine, David Geffen School of Medicine at UCLA, Los Angeles, California 90095, United States

**ABSTRACT** Root canal therapy (RCT) represents a standard of treatment that addresses infected pulp tissue in teeth and protects against future infection. RCT involves removing dental pulp comprising blood vessels and nerve tissue, decontaminating residually infected tissue through biomechanical instrumentation, and root canal obturation using a filler material to replace the space that was previously composed of dental pulp. Gutta percha (GP) is typically used as the filler material, as it is malleable, inert, and biocompatible. While filling the root canal space with GP is the standard of care for endodontic therapies, it has exhibited limitations including leakage, root canal reinfection, and poor mechanical properties. To address these challenges, clinicians have explored the use of alternative root filling materials other than GP. Among the classes of materials that are being explored as novel endodontic therapy platforms, nanodiamonds (NDs) may offer unique advantages due to their favorable properties, particularly for dental applications. These include versatile faceted surface chemistry, biocompatibility, and their role in improving mechanical properties, among others. This study developed a ND-embedded GP (NDGP) that was functionalized with amoxicillin, a broad-spectrum antibiotic commonly used for endodontic infection. Comprehensive materials characterization confirmed improved mechanical properties of NDGP over unmodified GP. In addition, digital radiography and microcomputed tomography imaging demonstrated that obturation of root canals with NDGP could be achieved using clinically relevant techniques. Furthermore, bacterial growth inhibition assays confirmed drug functionality of NDGP functionalized with amoxicillin. This study demonstrates a promising path toward NDGP implementation in future endodontic therapy for improved treatment outcomes.



Nanodiamond–Gutta Percha Biomaterials for Root Canal Therapy

**KEYWORDS:** nanomedicine · dentistry · biomaterials · drug delivery · root canal therapy · gutta percha · endodontics

Conventional root canal therapy (RCT) has been efficacious in salvaging teeth with a history of gross carious lesions, trauma, and fractures that lead to pulpal and periradicular infection.<sup>1–3</sup> During RCT, the infected or inflamed pulp tissue is removed, and the root canal space is cleaned and shaped before it is filled with gutta percha (GP), a rubber-based filling material with root canal cements. The final obturation step is a crucial step in endodontic therapy because the therapeutic outcome

depends on sealing the root canal space along the length of the root canal. While there are many benefits associated with saving natural dentition through endodontic therapies, RCTs may fail due to inadequate sealing of infected root canals, allowing for bacterial regrowth within the root canal system, causing apical periodontitis and abscess.

Although RCT employs powerful intracanal irrigants, *e.g.*, 6% NaOCl, to eradicate microbial infection, it is very difficult to achieve complete disinfection of the complex

\* Address correspondence to dho@dentistry.ucla.edu, nanoscientist@ucla.edu.

Received for review September 11, 2015 and accepted October 9, 2015.

Published online October 09, 2015  
10.1021/acsnano.5b05718

© 2015 American Chemical Society

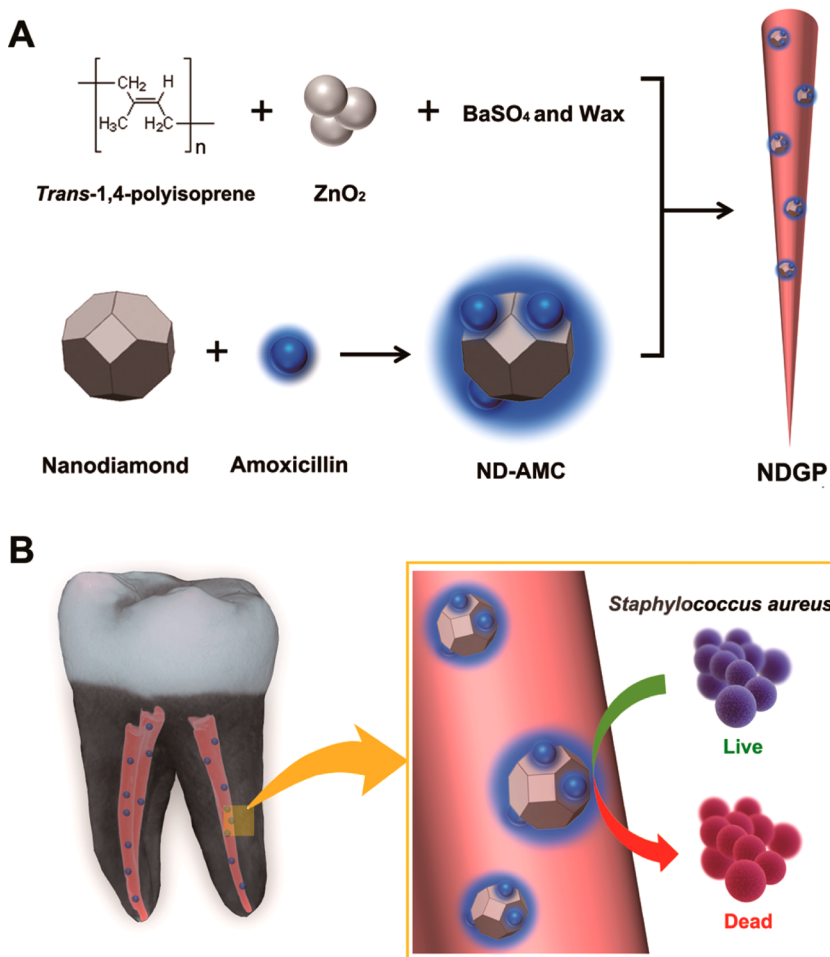


**Figure 1.** Schematic of NDGP embedded with ND-AMC conjugates. (A) Synthesis of NDGP. A polyisoprene solution was prepared by solvating *trans*-1,4-polyisoprene in chloroform at a 1:71 (w/w) ratio of polyisoprene to chloroform. Zinc oxide ( $ZnO_2$ ), barium sulfate ( $BaSO_4$ ), and wax were added to this solution at a 3.3:0.55:0.15 ratio. ND-AMC was then mixed into the polyisoprene solution, and the final mixture was lyophilized to obtain solid NDGP. (B) NDGP can prevent bacterial contamination after root canal therapy due to the antimicrobial properties of both ND and amoxicillin.

root canal anatomy.<sup>4,5</sup> Furthermore, secondary intra-canal structures, e.g., lateral canals and isthmuses, may harbor established bacterial biofilm and serve as a source of root canal reinfection, causing treatment failures. These lateral canals exist throughout most root canal structures and are poorly detectable in dental radiographs. Even if detected, lateral canals are often difficult to instrument, leaving the pre-existing bacterial biofilms untouched.

While GP offers numerous advantages, including biocompatibility, cost efficiency, ease of removal, and a long history of use, its inability to provide adequate seal to prevent bacterial percolation is a challenge in endodontic therapy. For instance, inadequate root canal seal around voids within the obturated root canal space may allow leakage due to absence of bonding between GP and the dentinal surface.<sup>6,7</sup> Such voids with leakage may allow regrowth of bacterial within the root canals, including those in dentinal tubules, and establish reinfection of the root canal space, causing treatment failures. To address these possibilities of root

canal reinfection, we harnessed the field of nanomedicine with a broad spectrum of powerful nanoparticle platforms for drug delivery, imaging, and other applications.<sup>8–13</sup> We developed a nanodiamond–gutta percha composite (NDGP) embedded with nanodiamond–amoxicillin (ND-AMC) conjugates (Figure 1A), which can reduce the likelihood of root canal reinfection and enhance the treatment outcomes. NDs are carbon nanoparticles that are approximately 4–6 nm in diameter; they are waste byproducts that are readily processed for biomedical applications.<sup>14–24</sup> Numerous studies have shown that NDs are biocompatible platforms for drug delivery and imaging, as they possess surface chemistries suited for electrostatic adsorption and/or covalent conjugation of various compounds.<sup>25–46</sup> Most importantly, NDs themselves have demonstrated antimicrobial activity.<sup>47–48</sup> Therefore, the use of biocompatible NDs to simultaneously sequester and localize the activity of amoxicillin as a model therapeutic, as well as confer enhanced mechanical properties to GP for improved ease of handling during obturation, provides

a translationally relevant route toward improving endodontic treatment outcomes.

Our NDGP platform integrates several important attributes into a single filler material. These attributes include improved mechanical properties, relative to those of unmodified GP, and antimicrobial activity against oral bacterial flora (Figure 1B). By taking advantage of the ND surface chemistry, a broad-spectrum antibiotic, such as amoxicillin, can be adsorbed to the ND surface (Figure 1A). Embedding amoxicillin-linked NDs into GP may facilitate the eradication of residual bacteria within the root canal system after completion of obturation. NDGP may also kill bacteria entering through the lateral canals following contact with ND–antibiotic agents. The homogeneous dispersion of NDs throughout the GP matrix also leads to an increase in toughness, as evidenced by mechanical tests comparing the tensile strength of unmodified GP and NDGP. Importantly, root canals were effectively obturated using traditional obturation techniques for both NDGP and unmodified GP. This was validated by performing a conventional lateral obturation technique on human teeth after root canal cleaning and shaping. A comparable quality and diagnostic capability of obturation between unmodified GP and NDGP was confirmed *via* digital radiography and micro-CT imaging.

## RESULTS AND DISCUSSION

**ND–Antibiotic Synthesis and Characterization.** Two samples of ND-AMC were synthesized by mixing amoxicillin and ND in 2.5 mM NaOH in two distinct ratios: (i) 5:2 w/w ND to amoxicillin (5:2 ND-AMC) and (ii) 5:3 w/w ND to amoxicillin (5:3 ND-AMC). After mixing, the ND-AMC samples were incubated at room temperature for 5–7 days to allow sufficient time for amoxicillin incorporation with ND.

Formation of the ND-AMC complex was assessed using dynamic light scattering (DLS) and  $\zeta$ -potential analysis. Amoxicillin sequestration by ND was accompanied by a marked increase in hydrodynamic size and decrease in  $\zeta$ -potential. The hydrodynamic size and  $\zeta$ -potential of unmodified ND were measured to be  $46.64 \pm 0.17$  nm and  $55.80 \pm 0.37$  mV, respectively (Figure 2A). In contrast, 5:2 ND-AMC had a hydrodynamic size of  $143.03 \pm 4.21$  nm and  $\zeta$ -potential of  $46.08 \pm 1.10$  mV, while 5:3 ND-AMC had a hydrodynamic size of  $151.53 \pm 1.22$  nm and  $\zeta$ -potential of  $40.57 \pm 2.94$  mV (Figure 2A).

The quantity of amoxicillin loaded onto the ND particles was calculated by subtracting the amount of unbound amoxicillin from the initial loading amount after completing ND-AMC synthesis. As shown in Figure 2B,  $1.30 \pm 0.02$  mg/mL of amoxicillin was loaded onto 5 mg/mL of ND from an amoxicillin loading concentration of 2 mg/mL (5:2 ND-AMC), while  $2.10 \pm 0.05$  mg/mL of amoxicillin was loaded onto 5 mg/mL

of ND from an amoxicillin loading concentration of 3 mg/mL (5:3 ND-AMC). These concentration values correspond to loading efficiencies of  $\sim 65\%$  for 5:2 ND-AMC and  $\sim 70\%$  for 5:3 ND-AMC, suggesting that ND-AMC synthesis generates amoxicillin-linked NDs.

It is important to note that mere sequestration of amoxicillin by ND is insufficient. The drug must be adsorbed strongly enough such that it does not immediately release after incorporation with ND. An immediate burst release of amoxicillin is obstructive to the combination of ND-AMC and GP, as the drug is lost before the NDGP composite can be synthesized. Cumulative amoxicillin release profiles showed that the amoxicillin was released from ND-AMC in a sustained manner over a week-long period, regardless of the initial amoxicillin concentration (Figure 2C). Due to its greater drug payload, the 5:3 ND-AMC sample released  $274.58 \pm 6.29$   $\mu$ g/mL of amoxicillin over this one-week period, a concentration greater than the  $218.96 \pm 37.86$   $\mu$ g/mL released by the 5:2 ND-AMC sample over the same duration. However, in terms of percentage release, the 5:3 ND-AMC sample eluted  $\sim 13.1\%$  of its total drug payload, whereas the 5:2 ND-AMC sample eluted  $\sim 16.8\%$  of its drug payload. Despite differences in total amounts of released drug, the percentage release values of 5:2 ND-AMC and 5:3 ND-AMC were comparably low, suggesting sustained adsorption of amoxicillin onto the ND surface. This interaction between amoxicillin and ND can prevent loss of amoxicillin during NDGP synthesis.

Fourier transform infrared (FTIR) spectroscopy analysis was performed as a final validation step for amoxicillin loading. Vibrational peaks corresponding to functional groups on ND, AMC, and ND-AMC were compared (Figure 2D). The ND and ND-AMC spectra shared similar peaks, including an O–H bending vibration peak at  $1632\text{ cm}^{-1}$  and C=O stretching vibration peaks from 1700 to  $1800\text{ cm}^{-1}$  corresponding to ketones, esters, lactones, and carboxylic acid groups found on ND surfaces. The spectra of amoxicillin and ND-AMC also overlapped at peaks associated with amoxicillin functional groups. Vibrational bands on the ND-AMC spectra from 800 to  $900\text{ cm}^{-1}$  represented bending vibrations of secondary and primary amine groups on amoxicillin. A series of small amoxicillin peaks from 1000 to  $1700\text{ cm}^{-1}$  are also found exclusively on the ND-AMC spectra and not the ND spectrum. These small vibrational peaks include C–H bending vibrations from 1220 to  $1250\text{ cm}^{-1}$ , NC–H and COOH bending vibrations from 1300 to  $1380\text{ cm}^{-1}$ , CH<sub>3</sub> bending vibrations from 1390 to  $1400\text{ cm}^{-1}$ , phenolic O–H bending vibrations from 1430 to  $1450\text{ cm}^{-1}$ , benzylic C=C stretching vibrations from 1500 to  $1590\text{ cm}^{-1}$ , and ketone C=O stretching vibrations from 1680 to  $1710\text{ cm}^{-1}$ . These FTIR data confirm successful loading of amoxicillin onto NDs.

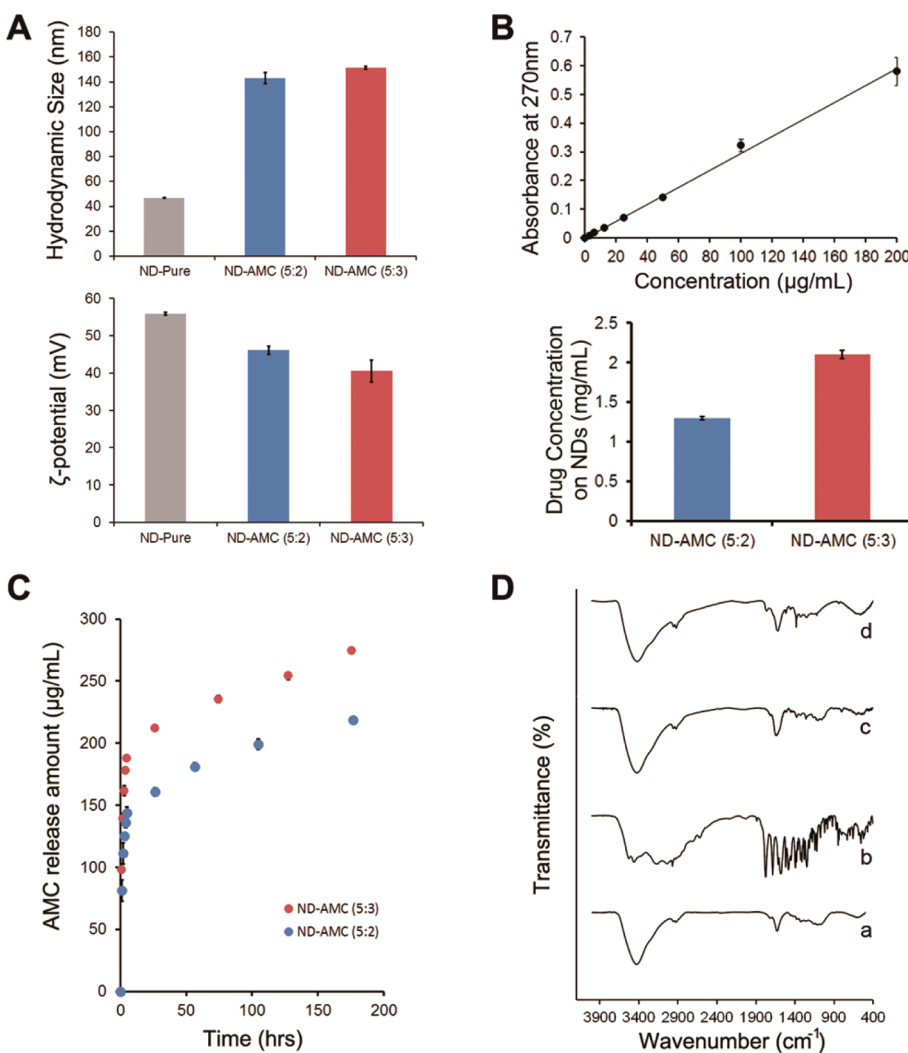


**Figure 2. Characterization of ND-AMC.** (A) Dynamic light scattering analyses and  $\zeta$ -potential measurements for unmodified ND (ND-Pure) and ND-AMC samples synthesized from a 5:2 w/w ratio of ND to amoxicillin (5:2 ND-AMC) and a 5:3 w/w ratio of ND to amoxicillin (5:3 ND-AMC). Top graph: Hydrodynamic sizes of ND-Pure, 5:2 ND-AMC, and 5:3 ND-AMC were measured to be  $46.64 \pm 0.17$ ,  $143.03 \pm 4.21$ , and  $151.53 \pm 1.22$  nm, respectively. Bottom graph:  $\zeta$ -potentials of ND-Pure, 5:2 ND-AMC, and 5:3 ND-AMC were measured to be  $55.80 \pm 0.37$ ,  $46.08 \pm 1.10$ , and  $40.57 \pm 2.94$  mV, respectively. (B) Standard curve for amoxicillin concentrations (top) and the final amount of amoxicillin successfully loaded onto NDs (bottom). Using the standard curve, the loading efficiency for ND-AMC was determined. For the 5:2 ND-AMC sample,  $1.30 \pm 0.02$  mg/mL of amoxicillin was loaded from an initial amoxicillin concentration of 2 mg/mL (~65% efficiency). For the 5:3 ND-AMC sample,  $2.10 \pm 0.05$  mg/mL of amoxicillin was loaded from an initial amoxicillin concentration of 3 mg/mL (~70% efficiency). (C) Cumulative amoxicillin release profiles for ND-AMC samples synthesized from 5:2 or 5:3 (w/w) ratios of ND to amoxicillin. For both samples, sustained amoxicillin release was observed for 1 week, with some burst release observed during hours 1–5. Although the 5:3 ND-AMC sample exhibits greater total drug release ( $274.58 \pm 6.29$   $\mu\text{g}/\text{mL}$ ) than the 5:2 ND-AMC sample ( $218.96 \pm 37.86$   $\mu\text{g}/\text{mL}$ ), the two samples released similar percentages of their respective amoxicillin payloads (~16.8% for 5:2 ND-AMC and ~13.1% for 5:3 ND-AMC). (D) FTIR spectra of (a) unmodified ND, (b) amoxicillin, (c) 5:2 ND-AMC, and (d) 5:3 ND-AMC. The FTIR spectra of both ND-AMC samples displayed C=C–H out-of-plane bending vibrations at  $820$ – $840$   $\text{cm}^{-1}$  and C=C stretching vibrations at  $1560$  and  $1603$   $\text{cm}^{-1}$ , which are well matched with similar peaks on the amoxicillin spectrum. A C=O stretching vibration found at  $1628$   $\text{cm}^{-1}$  on the spectra of both ND-AMC samples also matches well with a similar peak found on the unmodified ND spectrum.

**Preparation and Evaluation of an NDGP Composite.** In order to enhance the antimicrobial and mechanical properties of GP, amoxicillin-loaded NDs were embedded into the GP matrix. Briefly, the GP matrix was prepared by the composition of polyisoprene,  $\text{ZnO}_2$ ,  $\text{BaSO}_4$ , and wax with a conventional ratio of 3.3:0.55:0.15, respectively. After thoroughly mixing the components, amoxicillin-loaded NDs were dispersed by sonication, followed by overnight lyophilization until all solvents

were removed. After the preparation of NDGP, crucial physical properties for endodontic materials, including radiopacity and elastic modulus, were assessed.

In clinical procedures, radiopacity is a critically important property of root canal filling materials. In order to evaluate the quality of obturation, root canal fillers should be radiopaque for the clinicians to visualize the level of root canal obturation and the obturation quality. In order to determine the radiopacity of

NDGP, we compared the digital X-ray images of NDGP with those of unmodified GP (Figure 3A). Both NDGP (top in both images) and unmodified GP (bottom in both images) showed clear radiopaque X-ray images, which indicates that both materials have comparable radiopacities.

A major goal of the NDGP platform was to improve the mechanical properties of GP, which may lead to improved handling properties during clinical implementation. In general composite materials, additives (e.g., NDs) are associated with organic polymers, reinforcing the mechanical properties by enhancing the interface strength between the additives and polymer. We prepared NDGP with 5 and 10 wt % of NDs to elucidate the effect that NDs would have on the elastic modulus, tensile strength, 0.2% offset yield strength, and percent elongation of GP (Figure 3B–F).

From the initial straight portion of stress–strain curve, the elastic modulus of each sample was derived. As shown in Figure 3C, the addition of 5 and 10 wt % of ND into the GP matrix improves the elastic moduli by 49% and 247%, respectively. In addition, the tensile strength and 0.2% offset yield strength increased 74% and 34% for 5 wt % ND addition and 171% and 85% for 10 wt % ND addition, respectively (Figure 3D and E). However, percent elongation of GP was decreased by 11% upon 5 wt % ND addition and 24% upon 10 wt % ND addition (Figure 3F). Combined, these results showed that the incorporation of NDs into the GP matrix improved the elastic modulus and mechanical strength of the NDGP biomaterial with a minor loss of ductility.

**Antimicrobial Efficacy Studies Using NDGP.** The primary objective of this study was to confirm amoxicillin functionality following its loading onto ND and incorporation into NDGP. Various bacterial strains can be encountered during reinfection scenarios following root canal therapy. Therefore, a *Staphylococcus aureus* (*S. aureus*) strain (ATCC 6538) was selected as the model bacterium for this NDGP antimicrobial efficacy study, as it has been previously observed in endodontic reinfection cases.<sup>49–51</sup> Recent studies have shown that various *S. aureus* strains can express beta-lactamase, an enzyme that hydrolyzes beta-lactams.<sup>52</sup> Because of this beta-lactamase expression, reported minimum inhibitory concentrations (MICs) of amoxicillin against *S. aureus* 6538 have ranged from 31.250 to over 100 µg/mL.<sup>53,54</sup> For this efficacy study, an NDGP sample was generated with an initial ND:amoxicillin ratio of 5:6 (w/w), where 8 mg of drug was ultimately incorporated into the NDGP sample. This quantity of loaded amoxicillin far exceeds reported amoxicillin MICs for *S. aureus* 6538, and NDGP should exhibit an inhibitory effect against this particular strain of bacteria as long as drug functionality is preserved upon incorporation into NDGP.

Two avenues of antimicrobial activity are possible for this NDGP platform: (i) bacterial killing through

amoxicillin release from NDGP and/or (ii) contact-mediated inhibition upon bacterial deposition onto the NDGP surface. To determine whether or not amoxicillin is freely eluted from the NDGP composite, an agar diffusion test was conducted with unmodified GP and NDGP. Neither unmodified GP nor NDGP produced a zone of inhibition after incubating on a lawn of *S. aureus* for 24 h, indicating a negligible amount of amoxicillin elution from NDGP (Figure 4A). This was an important observation because avoidance of elution from NDGP was a prerequisite for contact-mediated inhibition, the desired mechanism of antimicrobial activity for our NDGP platform.

To determine the degree by which *S. aureus* was killed upon surface contact with NDGP, bacteria were deposited onto both unmodified GP and NDGP. Bacteria were visualized with a live/dead stain. After 70 h of contact, fluorescent images of both the unmodified GP surface and the NDGP surface were generated at 10× magnification. Unmodified GP exhibited no apparent inhibition of *S. aureus* (Figure 4B, row 1). In contrast, there was a significant amount of bacterial death on the NDGP surface (Figure 4B, row 2). Bacteria on the NDGP surface also formed large aggregates, whereas the bacteria on the GP surface remained dispersed. This effect may have been due to the bacteria's attempt to minimize exposure to the NDGP surface, hence reducing cell death.<sup>55,56</sup> When *S. aureus* was treated for 24 h with amoxicillin (150 µg/mL) or ND (10 mg/mL) alone, bacterial death was also observed, showing that *S. aureus* responds to both amoxicillin and ND treatment (Figure 4B, rows 3 and 4). Taken together, these results suggest that drug functionality was preserved during NDGP synthesis and that NDGP prevents bacterial contamination through a contact-mediated inhibition mechanism.

It should be mentioned that a key reason for the use of ND particles to sequester and localize amoxicillin activity and mediate contact-based inhibition is that the reduction of antibiotic elution mediated by the NDs may play an important role in reducing antibiotic resistance. In addition, the absence of drug elution coupled with contact-mediated inhibition reduces the dosage of amoxicillin that is loaded into the NDGP. At the same time, the NDs can play a structural role in enhancing the mechanical properties of the NDGP composite. To potentially accelerate NDGP translation toward clinical use, the use of carbon in the oral cavity and digestive tract has been demonstrated using activated charcoal tablets.<sup>57</sup> In addition, coupling antibiotics that have been approved for human use with NDs may serve as a promising route for first in-human studies of NDGP. As a novel material, the NDGP was designed to remain confined within the root canal to mediate contact-based inhibition. Therefore, the NDGP minimizes contact with dental tissue beyond

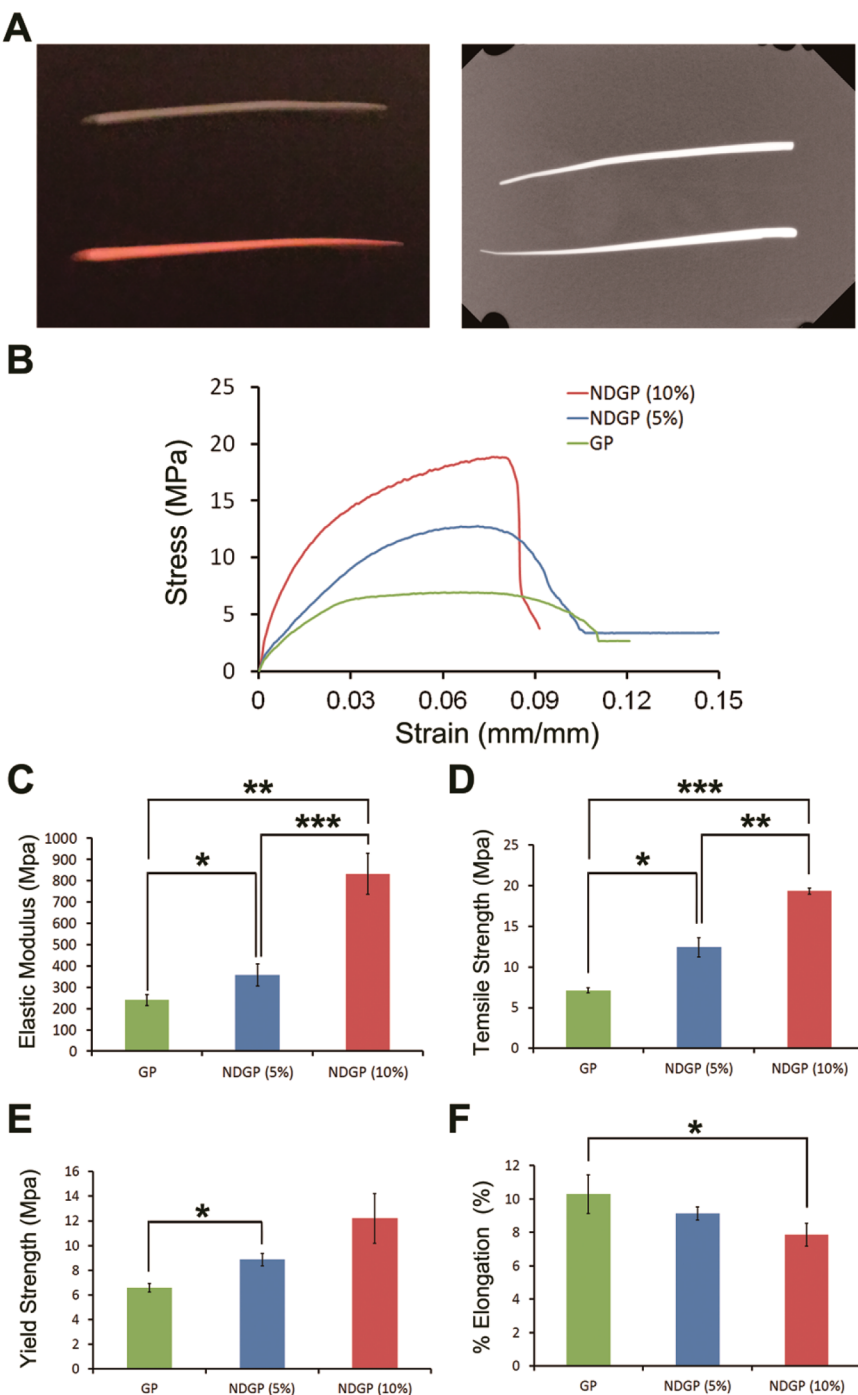


**Figure 3.** Radiopacity and mechanical properties of NDGP. (A) Left: Photograph of NDGP (top) and unmodified GP (bottom). Right: Digital X-ray image of NDGP (top) and unmodified GP (bottom). An X-ray image showed that the radiopacity of NDGP was comparable to that of unmodified GP. (B) Stress–strain curves of G, and NDGP (5 wt % ND, 10 wt % ND) obtained by tensile test. The tests were performed with a 0.3 cm/min strain rate with sample gauge lengths set at 0.89 cm. They clearly showed the areas under the curves of NDGPs (5% and 10%) are larger than unmodified GP, which means NDGPs are more mechanically robust than unmodified GP. (C) Elastic moduli of GP ( $240 \pm 26.3$  MPa), NDGPs with 5 wt % ND ( $357 \pm 52.0$  MPa), and NDGP with 10 wt % ND ( $833 \pm 96.5$  MPa) calculated by initial linear portions of stress–strain curves. Data are represented as mean  $\pm$  SD; \*,  $p < 0.05$ ; \*\*,  $p < 0.01$ ; \*\*\*,  $p < 0.005$  ( $n = 3$ ). (D) Tensile strengths of GP ( $7 \pm 0.3$  MPa), NDGP with 5 wt % ND ( $12 \pm 1.2$  MPa), and NDGP with 10 wt % ND ( $19 \pm 0.3$  MPa) obtained from the highest stress point. Data are represented as mean  $\pm$  SD; \*,  $p < 0.05$ ; \*\*,  $p < 0.005$ ; \*\*\*,  $p < 0.00001$  ( $n = 3$ ). (E) 0.2% offset yield strengths of GP ( $7 \pm 0.3$  MPa), NDGP with 5 wt % ND ( $9 \pm 0.5$  MPa), and NDGP with 10 wt % ND ( $12 \pm 2.0$  MPa) obtained from stresses that correspond to the points of intersections of a stress–strain curve and lines that are parallel to the initial part of straight lines. It can be used to approximately determine elastic limits. Data are represented as mean  $\pm$  SD; \*,  $p < 0.005$  ( $n = 3$ ). (F) Percent elongation of GP ( $10 \pm 1.2$  MPa), NDGP with 5 wt % ND ( $9 \pm 0.4$  MPa), and NDGP with 10 wt % ND ( $8 \pm 0.7$  MPa) measured by changes in lengths from the original length. Data are represented as mean  $\pm$  SD; \*,  $p < 0.05$  ( $n = 3$ ).

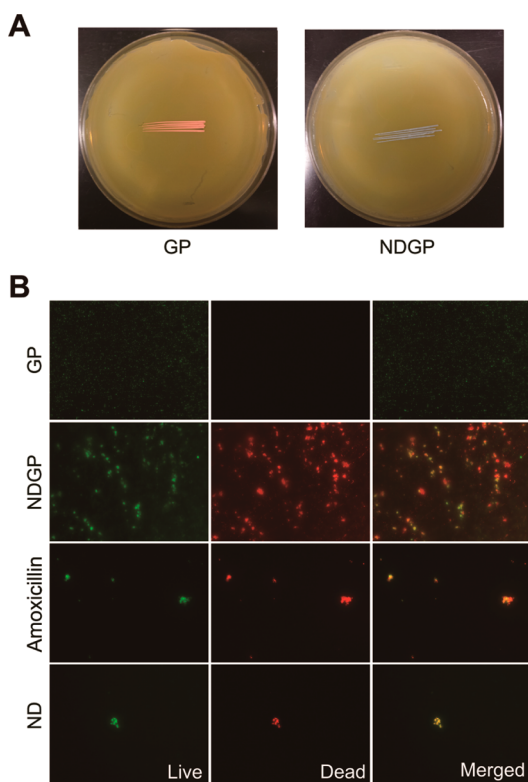


**Figure 4. Comparison of NDGP antimicrobial properties with that of unmodified GP.** (A) Agar diffusion test conducted with disks of unmodified GP and NDGP. After 24 h of incubation, there was no observable zone of inhibition around either disk, suggesting negligible amoxicillin release from NDGP. Therefore, bacterial inhibition was likely achieved through a contact-mediated mechanism. (B) Representative live/dead strains of bacteria-coated GP and bacteria-coated NDGP with relevant amoxicillin-only and ND-only controls. The merged images (right column) were separated into red and green channels during ImageJ processing to distinguish between dead (red fluorescence, middle column) and live (green fluorescence, left column) bacteria. First row: *S. aureus* 6538 in contact with unmodified GP did not undergo cell death, as evidenced by the lack of red fluorescent signal (middle). Live bacteria were observed (left). The merged image (right) was taken at 10 $\times$  magnification after 70 h of surface contact. Second row: *S. aureus* 6538 in contact with NDGP experienced significant cell death, as indicated by the presence of red fluorescent staining (middle). Live bacteria were also present (left). Bacterial clumping was observed. This behavior may be an attempt by the bacteria to reduce exposure to the NDGP surface. The merged image (right) was taken at 10 $\times$  magnification after 70 h of surface contact. Third row: A saline solution containing 150  $\mu$ g/mL of amoxicillin induced cell death in *S. aureus* 6538 colonies. The merged image (right) was taken at 60 $\times$  magnification after 24 h of treatment. The 60 $\times$  image is representative of bacterial viability levels observed under 10 $\times$  magnification. Fourth row: A saline solution containing 10 mg/mL nanodiamond also induced bacterial death in *S. aureus* 6538 colonies. The merged image (right) was taken at 60 $\times$  magnification after 24 h of treatment. The 60 $\times$  image is representative of bacterial viability levels observed under 10 $\times$  magnification.

the apex of the tooth that is sometimes observed with conventional sealers. Furthermore, adding a drug directly into the sealer would likely result in drug elution and depletion following burst release, which is not an intended use of the NDGP platform. Subsequent

iterations of NDGP may potentially explore the use of emerging antibacterial agents.<sup>58–62</sup>

**X-ray Imaging of Root Canal Obturation.** Extracted human teeth obturated with unmodified GP and NDGP were imaged using digital radiography (XDR) to compare the quality of obturation between the two different materials. Digital X-ray imaging provides clinicians with a preliminary two-dimensional view of obturated root canals, allowing for detection of voids and quality of the root canal fill.<sup>63–65</sup> Root canal obturation of human teeth with NDGP revealed no apparent void formation after conventional technique, e.g., lateral condensation,<sup>66</sup> particularly in the critical apical third region (Figure 5). This suggests that NDGP can be used for obturation of root canals using conventional obturation techniques commonly used in clinical settings. In addition to the comparable quality of obturation with NDGP and unmodified GP, the radiopacities of both materials were indistinguishable (Figure 5). These images suggest that NDGP could be clinically implemented using conventional endodontic therapy procedures.

**Microcomputed Tomography Imaging of Root Canal Obturation.** Although digital radiography is used as a clinical standard for determining the quality of obturation and prognosis of endodontic therapies, periapical radiography depicts only a two-dimensional view of the complex root canal structures. We also employed imaging with microcomputed tomography ( $\mu$ CT) to assess the effectiveness of NDGP and unmodified GP in root canal obturation and assessment of void formation. While  $\mu$ CT imaging cannot be utilized during RCT to assess the quality of obturation, enhanced resolution offered by  $\mu$ CT provided important insight as part of this study to compare the effectiveness of NDGP and unmodified GP for root canal obturation. A minimal number of small voids were observed in the canals following obturation with NDGP, comparable to the number of voids also observed in those obturated with unmodified GP (Figure 5). The minimal voids present in the NDGP-filled tooth were in the middle third of the canal, which is a clinically acceptable criteria for a successful root canal treatment.

## CONCLUSION

This study demonstrated that functionalizing conventional GP cones with amoxicillin-loaded NDs may increase the success rate of endodontic therapies by eliminating pre-existing microbes and preventing reinfection of the root canal system. The mechanical robustness of GP was also increased upon ND incorporation, improving the handling properties during clinical implementation. Future studies will be useful in enhancing the GP interface with the surrounding tooth structure to ultimately improve fracture resistance in weakened endodontically treated teeth. Because of its antimicrobial properties and increased durability,

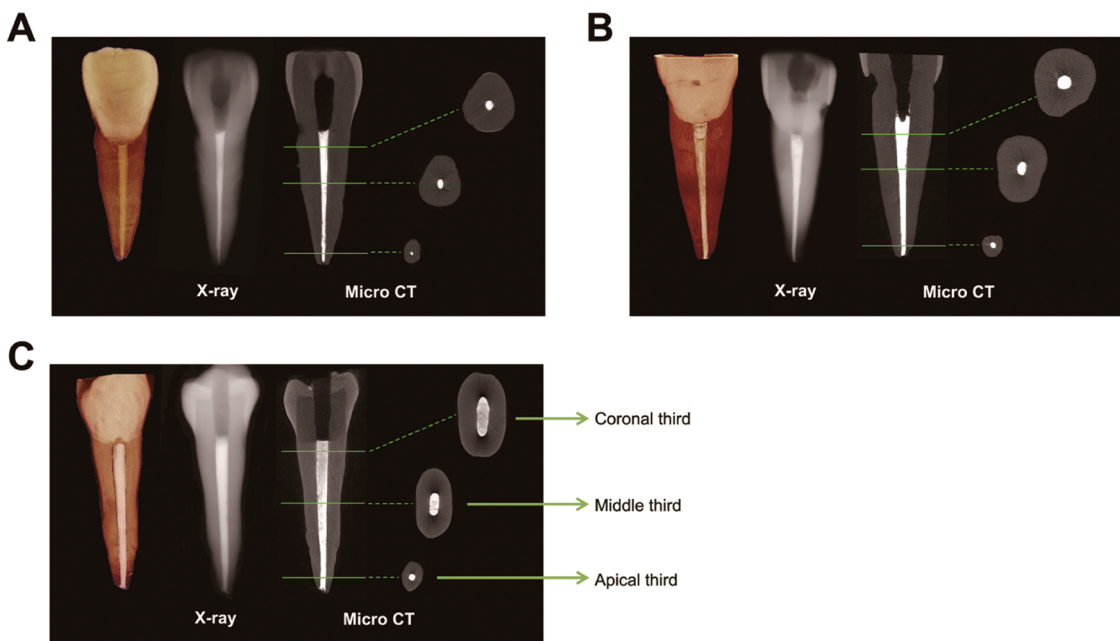


**Figure 5.** X-ray and microCT ( $\mu$ CT) images of patient-derived teeth samples obturated with unmodified GP and NDGP. (A) Central incisor prepared and obturated with unmodified GP. Left: Three-dimensional rendering of the GP-filled central incisor generated from a  $\mu$ CT image. Middle: A bucco-lingual X-ray view of the incisor revealed no visible voids within the obturated canal. Right:  $\mu$ CT imaging of GP-filled central incisor revealed no visible voids within the apical region of the obturated canal, although minor voids are present in the middle third of the obturated canal. Coronal, middle, and apical cross sections do not show any voids. (B) Central incisor prepared and obturated with NDGP. Left: Three-dimensional rendering of the NDGP-filled central incisor generated from a  $\mu$ CT image. Middle: A bucco-lingual X-ray view of the incisor also revealed no visible voids within the apical region of the obturated canal and minor voids in the middle third region. There were no discernible differences between the X-ray images of the GP-filled central incisor and the NDGP-filled central incisor. Right:  $\mu$ CT imaging of the NDGP-filled central incisor revealed no visible voids within the obturated canal. Coronal, middle, and apical cross sections also contained no voids. There were no discernible differences between the  $\mu$ CT images of the GP-filled central incisor and the NDGP-filled central incisor. (C) Premolar prepared and obturated with NDGP. Left: Three-dimensional rendering of the NDGP-filled premolar generated from a  $\mu$ CT image. Middle: A bucco-lingual X-ray view of the incisor revealed no visible voids within the obturated canal. Right:  $\mu$ CT imaging of the NDGP-filled premolar revealed no visible voids even within the obturated oval canal. Coronal, middle, and apical cross sections also contained no voids.

NDGP may enhance the success rate of conventional endodontic therapies and reduce the need for additional treatments, including retreats and apical surgeries.

Because NDGP is compatible with traditional obturation techniques, subsequent studies will focus on the clinical validation of NDGP.

## MATERIALS AND METHODS

**Materials.** NDs were purchased from the NanoCarbon Research Institute Co., Ltd. (Nagano, Japan) and used to prepare a 50 mg/mL aqueous ND stock solution. Phosphate buffer saline (PBS) was purchased from Thermo Fisher Scientific (Canoga Park, CA, USA), and fetal bovine serum (FBS) was purchased from Gemini Bio Products (West Sacramento, CA, USA). Amoxicillin, *trans*-1,4-polyisoprene, zinc oxide ( $ZnO_2$ ), barium sulfate ( $BaSO_4$ ), sodium hydroxide (NaOH), and chloroform were purchased from Sigma-Aldrich (St. Louis, MO, USA). Unmodified gutta percha points were purchased from SybronEndo (Glendora, CA, USA). Microcon-30 centrifugal filters were purchased from Merck Millipore Ltd. (Tullagreen, Carrigtwohill, IRL). For antimicrobial efficacy studies, *Staphylococcus aureus* was purchased from the American Type Culture Collection (ATCC 6538, Manassas, VA, USA). Soybean-casein digest medium was purchased from Becton, Dickinson and Company (Franklin Lakes, NJ, USA). Live/dead *BacLight* viability assay reagent was purchased from Thermo Fisher Scientific (catalog number L-7012). The ND stock solution was sterilized prior to further experimentation. All other reagents were used without further treatment.

**Synthesis and Characterization of ND-AMC Conjugates.** ND-AMC was synthesized by mixing NDs with amoxicillin at 5:2 and 5:3 (w/w)

ratios of ND to AMC in 2.5 mM NaOH. The mixture was vortexed and incubated for 5–7 days at room temperature. After incubation, the mixture was centrifuged down and washed with deionized water. The final product was collected via centrifugation at 20000g for 20 min and resuspended in water at a ratio of 5:1 (w/v) ND to water. To quantify amoxicillin loading onto ND, the concentration of unbound amoxicillin recovered after the washing process was used to calculate amoxicillin loading efficiency. The absorbance of the recovered amoxicillin supernatant was measured by UV-vis spectroscopy at 270 nm. The concentration of unbound amoxicillin in the supernatant was calculated from an amoxicillin standard curve with an amoxicillin concentration range of 0 to 200  $\mu$ g. The amount of unbound amoxicillin was subtracted from the amount loaded to determine the concentration of amoxicillin incorporated onto ND.

To verify amoxicillin binding to ND, Fourier transform infrared spectroscopy was performed with a PerkinElmer FTIR Spectrum 2000 (PerkinElmer, Waltham, MA, USA) over a wavenumber range of 400–4000  $\text{cm}^{-1}$ . A 2 mg amount of lyophilized ND-AMC samples was mixed with 100 mg of potassium bromide (KBr) powder, and the mixed powder samples were pressed to a thin disc for FTIR analysis. The FTIR spectra were recorded with a resolution of 1  $\text{cm}^{-1}$  and an accumulation of

64 scans. The hydrodynamic size and  $\zeta$ -potential of ND and ND-AMC suspensions ( $0.2\text{--}0.3\text{ mg mL}^{-1}$ ) were also measured with a Zetasizer Nano ZS (Malvern Instruments, United Kingdom). Hydrodynamic size measurements were performed at  $25^\circ\text{C}$  with a  $173^\circ$  backscattering angle. At least three size measurements were performed. The mean hydrodynamic size and its standard deviation were calculated by averaging the reported z-average size values and determining their standard deviation. The  $\zeta$ -potential was also measured at  $25^\circ\text{C}$  in automatic mode.

**Quantifying Drug Release from ND-AMC Conjugates.** Amoxicillin release experiments were performed in PBS solutions containing 0.5% v/v FBS. A 1 mL amount of ND-AMC solution was centrifuged for 20 min at  $14000\text{g}$  to obtain an ND-AMC pellet. This ND-AMC pellet was resuspended in 1 mL of 0.5% v/v FBS/PBS solution by gentle pipetting, followed by incubation for 1 h at  $37^\circ\text{C}$ . At each predetermined time point, the ND-AMC solution was centrifuged for 20 min at  $14000\text{g}$ , the supernatant was recovered, and the pellet was resuspended in 1 mL of PBS solution and incubated at  $37^\circ\text{C}$  until the next time point. At the next time point, this procedure was repeated.

To determine the amount of amoxicillin released at each time point, the recovered supernatant was filtered with Microcon-30 centrifugal filters to remove FBS. The absorbance value of the amoxicillin-containing supernatant was subsequently measured with a UV-vis spectrophotometer. The concentration of amoxicillin in the supernatant was calculated according to an amoxicillin standard curve derived from the same release media. Cumulative amoxicillin release profiles were generated by plotting cumulative amoxicillin concentration release (measured in  $\mu\text{g/mL}$ ) against predetermined time points (measured in hours).

**Synthesis and Characterization of NDGP.** Gutta percha functionalized with ND-AMC was synthesized by mixing polyisoprene,  $\text{ZnO}_2$ ,  $\text{BaSO}_4$ , wax, and ND-AMC. First, polyisoprene was solvated in chloroform at a ratio of 1:71 (w/w) of polyisoprene to chloroform.  $\text{ZnO}_2$ ,  $\text{BaSO}_4$ , and wax were then added to the polyisoprene solution at a ratio of 3.3:0.55:0.15, respectively, with 15 min of sonication after the addition of each component. Lyophilized ND-AMC was then dispersed and sonicated into the polyisoprene solution for 5 min to disperse any ND-AMC aggregates. The final solution was lyophilized overnight. After lyophilization, 25–30 mg of solid NDGP was heated at  $90^\circ\text{C}$  and molded into cones. NDGP was molded into fine-tipped cones, to mimic the shape of accessory cones, using a manual rolling procedure. However, further translation of these NDGP cones will involve the use of industry-standard scalable manufacturing protocols for consistent/automated NDGP synthesis.

To measure the mechanical properties of GP and NDGP, an Instron Universal Testing Machine (model 5564, Instron, Canton, MA, USA) was used. The tests were performed with a 0.3 cm/min strain rate with sample gauge lengths set at 0.89 cm. All cross-sectional areas were calculated from the diameter of each GP or NDGP cone. The elastic modulus of each sample was calculated from the initial straight portion of the sample's respective stress-strain curve.

**Validating Bacterial Response to Amoxicillin and ND Treatment.** *S. aureus* was grown in soybean-casein digest medium under aerobic conditions at  $37^\circ\text{C}$  until late log phase. Amoxicillin and ND were solvated in 0.85% w/v NaCl solutions at concentrations of  $150\text{ }\mu\text{g/mL}$  and  $10\text{ mg/mL}$ , respectively. A different dose of amoxicillin was utilized for the antibacterial response studies since the individual NDGP cones were loaded with lower amoxicillin dosages for contact-mediated inhibition. Confirmation of drug activity was performed on larger agar plates and was thus performed using a larger NDGP sample. The bacteria were resuspended in both solutions and incubated for 24 h. After 24 h, live/dead BacLight viability assay reagent was added to the bacterial suspensions according to the manufacturer's protocol. A  $10\text{ }\mu\text{L}$  portion of both the amoxicillin-treated bacterial suspension and the ND-treated amoxicillin bacterial suspension were dropped onto glass microscope slides. Glass coverslips were placed onto the drops, and the slides were sealed with nail polish. The slides were visualized with an Olympus IX81 fluorescent microscope (Olympus, Tokyo, Japan) at  $60\times$  magnification. Fluorescent images were processed

with ImageJ software (National Institutes of Health, Bethesda, MD, USA).

**Evaluating NDGP Drug Release and Antimicrobial Activity.** For this study, ND-AMC was synthesized by mixing a 5:6 (w/w) ratio of ND and amoxicillin instead of the original 5:2 or 5:3 (w/w) ratio. The loading efficiency of the amoxicillin was calculated as previously described, and the ND-AMC conjugates were incorporated with GP to synthesize NDGP containing 8 mg of amoxicillin. To assess drug release from NDGP, *S. aureus* was cultured in soybean-casein digest medium under aerobic conditions at  $37^\circ\text{C}$  until late log phase. Then  $200\text{ }\mu\text{L}$  of bacterial suspension was dropped onto soybean-casein digest agar plates and spread evenly over the entire plate. The plates were incubated at  $37^\circ\text{C}$  until a uniform lawn of bacteria was formed. An agar diffusion test was performed by pressing circular disks of unmodified GP and NDGP into the agar plates. After incubating for 24 h, the agar plates were checked for zones of inhibition.

To assess the viability of bacteria in direct contact with the NDGP surface, *S. aureus* was cultured in soybean-casein digest medium under aerobic conditions at  $37^\circ\text{C}$  until late log phase. The bacteria were resuspended in 0.85% w/v NaCl, and live/dead BacLight viability assay reagent was added to the bacterial suspension according to the manufacturer's protocol. Flat disks of unmodified GP and NDGP (5:6 w/w ND to AMC, synthesized as previously described) were attached to glass microscope slides. A  $20\text{ }\mu\text{L}$  amount of bacterial suspension was pipetted onto the NDGP and GP surfaces. Glass coverslips were placed on the disks to evenly distribute the bacterial suspension. The slides were sealed with nail polish and incubated for 70 h. After incubation, the bacteria-coated surfaces of NDGP and unmodified GP were visualized with an Olympus IX81 fluorescent microscope at  $10\times$  magnification. Fluorescent images were processed with ImageJ software.

**X-ray Imaging.** Digital radiograph images were taken with size 2 XDR Digital Intraoral sensors (XDR Radiology, Los Angeles, CA, USA). The images were then transmitted and analyzed by the XDR program. The patient-derived teeth samples were radiographed at 0.016 Gy. This served as a clinically relevant level of radiation that is typically observed for a digital periapical radiograph during a conventional root canal procedure. The X-ray source–object and object–sensor distances were kept constant for all exposures per conventional sample testing protocols.

**Computed Tomography Imaging.** Teeth samples were imaged using a SkyScan 1172  $\mu\text{CT}$  scanner (Bruker, Billerica, MA, USA) at  $20\text{ }\mu\text{m}$  resolution, utilizing 55 kVp,  $181\text{ }\mu\text{A}$ , and 0.5 Al filtration. Volumetric image data were converted to DICOM format and imported into the Dolphin Imaging software (Dolphin Imaging & Management Solutions, Chatsworth, CA, USA) to generate 3D and multiplanar reconstructed images.

**Selection and Preparation of Patient-Derived Teeth Samples.** Patient-derived teeth samples were obtained in accordance with an approved Institutional Review Board protocol (IRB #13-000241). The extracted teeth were screened by digital radiography. Challenging cases and teeth with multiple canals (*i.e.*, root curvature position and extent, pulp stones, calcification of canals, C-shaped canals, open apex, and root resorption) were excluded so that the level of expertise of the operator did not play a factor in the success of the root canal treatment. Out of 126 teeth, 20 teeth were radiographically assessed, out of which two central incisors and one maxillary second premolar, all single-canaled, were chosen to be obturated. Two central incisors were chosen for comparison in obturation between NDGP and unmodified GP. In addition, a maxillary premolar was also chosen to demonstrate the quality of the obturation of NDGP in an oval canal. One operator performed the endodontic procedure for all three teeth to reduce technical error. All procedures were done mounted in Acadental ModuPRO endodontic typodonts (Acadental, Overland Park, KS, USA) to simulate clinical situations as accurately as possible.

**Cleaning and Shaping of Extracted Human Teeth.** An access cavity was prepared with #2 and #4 round burs. After the bur penetrated into the pulp chamber, the roof of the chamber was carefully removed. The Caulk Endo Z bur (Dentsply International, York, PA, USA) was used to create and refine the proper

border of the chamber. The working lengths were approximated by using the ruler feature on the XDR digital radiography program. The initial apical file (IAF) was determined with a stainless steel (SS) file to reach 0.5 mm from the radiographic apex. A 10 SS file was initially used, and then the file size was increased until it fit snugly to working length. The IAFs for the following teeth A, B, and C were #15 (SS), #20 (SS), and #20 (SS), respectively. A radiograph was taken to confirm that the working length was reached. Then, coronal flaring was achieved with Gates-Glidden 4, 3, and 2 (Dentsply International) in a crown-down technique. Afterward, a circumferential filing technique was used until the IAF file became loose in the canal, and then filing was continued with the next larger file until the file became loose. This technique was continued for the subsequent files until the master apical file (MAF) was achieved. The MAFs of teeth A, B, and C were #30, #45, and #45. A radiograph was taken to confirm that the working length was reached.

Overall flaring was achieved in a crown-down technique using rotary NiTi Profile ISO files (Dentsply International). Starting with size 30/0.06 taper, 25/0.06 and 25/0.04 were used in sequence with pencil pressure until about 1 mm from the working length was achieved. An automated torque control motor was used with a speed set to 300 for all rotary files. The torque was set to 2.5, 0.8, and 1.7, respectively. The MAFs were then used in circumferential filing to remove debris and blend the apical and coronal flares evenly. After every file, the canal was thoroughly irrigated with 5.25% sodium hypochlorite (NaOCl) to remove debris so that apical blockages do not occur. Root canal preparation cream (Premier, Plymouth Meeting, PA, USA) was frequently used as an intracanal lubricant. Patency was maintained throughout each step to prevent debris accumulation in the apices.

**Occlusion of Root Canals in Extracted Human Teeth.** The lateral condensation obturation technique was used. After thoroughly drying the canal with paper points, master cones were selected. Master cones all had tugback and reached working length after radiographic assessment. The master cone sizes of teeth A, B, and C were 40, 45, and 45. After eugenol Roth sealer (Roth International Ltd., Chicago, IL, USA) was applied into the canal with the MAF, the master cone was inserted and then the spreader was inserted vertically until firm resistance for around 5–10 s and then withdrawn. While three regular gutta percha medium-fine (MF) accessory cones were used to fill tooth A, three MF NDGP accessory cones were also used to fill teeth B and C. After radiographic confirmation that there were no apical voids, the Glick instrument was heated at its end and then the canal orifices were sealed off. While the gutta percha was still warm, an unheated plunger was used to apply a vertical condensation force. Then, about 1–2 mm of excess gutta percha was removed below the cementoenamel junction, and the remaining sealer in the pulp chamber was cleaned with alcohol on a cotton pellet. The teeth were then taken out of the ModuPRO segment for a final radiograph to assess the quality of obturation.

**Statistical Analysis.** Experiments were conducted in triplicate. Quantifiable results were averaged, and standard deviations were calculated. Analysis of mechanical differences between GP and NDGP was conducted with an unpaired, two-tail Student's *t* test. A *p*-value of <0.05 was considered statistically significant.

**Conflict of Interest:** The authors declare the following competing financial interest(s): D.K.L., S.V.K., A.N.L., A.Y., and D.H. are co-inventors of a provisional patent pertaining to nanodiamond-based biomaterials for dental applications.

**Acknowledgment.** The authors gratefully acknowledge N. Gomez for helpful discussions, and Y. Zhang and B. Wu for the use of their Instron Universal Testing Machine. D.H. gratefully acknowledges support from the National Science Foundation CAREER Award (CMMI-1350197), Center for Scalable and Integrated NanoManufacturing (DMI-0327077), CMMI-0856492, DMR-1343991, V Foundation for Cancer Research Scholars Award, Wallace H. Coulter Foundation Translational Research Award, National Cancer Institute grant U54CA151880 (the content is solely the responsibility of the authors and does not necessarily represent the official views of the National

Cancer Institute or the National Institutes of Health), Society for Laboratory Automation and Screening Endowed Fellowship, and Beckman Coulter Life Sciences.

## REFERENCES AND NOTES

- Friedman, C. M.; Sandrik, J. L.; Heuer, M. A.; Rapp, G. W. Composition and Mechanical Properties of Gutta-Percha Endodontic Points. *J. Dent. Res.* **1975**, *54*, 921–925.
- Ehrmann, E. H.; Boqinst, A.; Falna, S. The Sterilization of Gutta-Percha Points. *Aust. Dent. J.* **1975**, *20*, 157–160.
- Johnson, W. B. A New Gutta-Percha Technique. *J. Endod.* **1978**, *4*, 184–188.
- Kandaswamy, D.; Venkateshbabu, N. Root Canal Irrigants. *J. Conservative Dent.* **2010**, *13*, 256–264.
- Zehnder, M. Root Canal Irrigants. *J. Endod.* **2006**, *32*, 389–398.
- Soo, W. K. M.; Thong, Y. L.; Gutmann, J. L. A Comparison of Four Gutta-Percha Filling Techniques in Simulated C-Shaped Canals. *International Endodontic Journal* **2015**, *48*, 736–746.
- Clinton, K.; Himel, V. T. Comparison of a Warm Gutta-Percha Obturation Technique and Lateral Condensation. *J. Endod.* **2001**, *27*, 692–695.
- Peppas, N. A.; Hilt, J. Z.; Khademhosseini, A.; Langer, R. Hydrogels in Biology and Medicine: From Molecular Principles to Bionanotechnology. *Adv. Mater.* **2006**, *18*, 1345–1360.
- Farokhzad, O. C.; Jon, S.; Khademhosseini, A.; Tran, T.-N. T.; LaVan, D. A.; Langer, R. Nanoparticle-Aptamer Bioconjugates A New Approach for Targeting Prostate Cancer Cells. *Cancer Res.* **2004**, *64*, 7668–7672.
- Eltoukhy, A. A.; Chen, D.; Alabi, C. A.; Langer, R.; Anderson, D. G. Degradable Terpolymers with Alkyl Side Chains Demonstrate Enhanced Gene Delivery Potency and Nanoparticle Stability. *Adv. Mater.* **2013**, *25*, 1487–1493.
- Gaharwar, A. K.; Patel, A.; Dolatshahi-Pirouz, A.; Zhang, H.; Rangarajan, K.; Ivgilia, G.; Shin, S.-R.; Hussain, M. A.; Khademhosseini, A. Elastomeric Nanocomposite Scaffolds Made from Poly(Glycerol Sebacate) Chemically Cross-linked with Carbon Nanotubes. *Biomater. Sci.* **2015**, *3*, 46–58.
- O'Brien, M. N.; Jones, M. R.; Lee, B.; Mirkin, C. A. Anisotropic Nanoparticle Complementarity in DNA-Mediated Co-Crystallization. *Nat. Mater.* **2015**, *14*, 833–839.
- Dhar, S.; Daniel, W. L.; Giljohann, D. A.; Mirkin, C. A.; Lippard, S. J. Polyvalent Oligonucleotide Gold Nanoparticle Conjugates As Delivery Vehicles for Platinum (IV) Warheads. *J. Am. Chem. Soc.* **2009**, *131*, 14652–14653.
- Lam, R.; Chen, M.; Pierstorff, E.; Huang, H.; Osawa, E.; Ho, D. Nanodiamond-Embedded Microfilm Devices for Localized Chemotherapeutic Elution. *ACS Nano* **2008**, *2*, 2095–2102.
- Manus, L. M.; Mastarone, D. J.; Waters, E. A. I.; Zhang, X.-Q.; Schultz-Sikma, E. A.; MacRenaris, K. W.; Ho, D.; Meade, T. J. Gd(III)-Nanodiamond Conjugates for MRI Contrast Enhancement. *Nano Lett.* **2010**, *10*, 484–489.
- Chow, E. K.; Zhang, X.-Q.; Chen, M.; Lam, R.; Robinson, E.; Huang, H.; Schaffer, D.; Osawa, E.; Goga, A.; Ho, D. Nanodiamond Therapeutic Delivery Agents Mediate Enhanced Chemoresistant Tumor Treatment. *Sci. Transl. Med.* **2011**, *3*, 73ra21.
- Smith, A. H.; Robinson, E. M.; Zhang, X.-Q.; Chow, E. K.; Lin, Y.; Osawa, E.; Xi, J.; Ho, D. Triggered Release of Therapeutic Antibodies from Nanodiamond Complexes. *Nanoscale* **2011**, *3*, 2844–2848.
- Chow, E. K.-H.; Ho, D. Cancer Nanomedicine: From Drug Delivery to Imaging. *Sci. Transl. Med.* **2013**, *5*, 216rv4.
- Moore, L.; Chow, E. K.-H.; Osawa, E.; Bishop, J. M.; Ho, D. Diamond-Lipid Hybrids Enhance Chemotherapeutic Tolerance and Mediate Tumor Regression. *Adv. Mater.* **2013**, *25*, 3532–3541.
- Xi, G.; Robinson, E.; Mania-Farnell, B.; Vanin, E. F.; Shim, K.-W.; Takao, T.; Allender, E. V.; Mayanil, C. S.; Soares, M. B.; Ho, D.; et al. Convection-Enhanced Delivery

- of Nanodiamond Drug Delivery Platforms for Intracranial Tumor Treatment. *Nanomedicine* **2014**, *10*, 381–391.
21. Toh, T.-B.; Lee, D.-K.; Hou, W.; Abdullah, L. N.; Nguyen, J.; Ho, D.; Chow, E. K.-H. Nanodiamond–Mitoxantrone Complexes Enhance Drug Retention in Chemoresistant Breast Cancer Cells. *Mol. Pharmaceutics* **2014**, *11*, 2683–2691.
  22. Kim, H.-J.; Zhang, K.; Moore, L.; Ho, D. Diamond Nanogel-Embedded Contact Lenses Mediate Lysozyme-Dependent Therapeutic Release. *ACS Nano* **2014**, *8*, 2998–3005.
  23. Wang, X.; Low, X. C.; Hou, W.; Abdullah, L. N.; Toh, T. B.; Mohd Abdul Rashid, M.; Ho, D.; Chow, E. K.-H. Epirubicin-Adsorbed Nanodiamonds Kill Chemoresistant Hepatic Cancer Stem Cells. *ACS Nano* **2014**, *8*, 12151–12166.
  24. Faklaris, O.; Joshi, V.; Irinopoulou, T.; Tauc, P.; Sennour, M.; Girard, H.; Gesset, C.; Arnault, J.-C.; Thorel, A.; Boudou, J.-P.; et al. Photoluminescent Diamond Nanoparticles for Cell Labeling: Study of the Uptake Mechanism in Mammalian Cells. *ACS Nano* **2009**, *3*, 3955–3962.
  25. Barnard, A. S. Self-Assembly in Nanodiamond Agglutinates. *J. Mater. Chem.* **2008**, *18*, 4038–4041.
  26. Barnard, A. S. Diamond Standard in Diagnostics: Nanodiamond Biolabels Make Their Mark. *Analyst* **2009**, *134*, 1751–1764.
  27. Adnan, A.; Lam, R.; Chen, H.; Lee, J.; Schaffer, D. J.; Barnard, A. S.; Schatz, G. C.; Ho, D.; Liu, W. K. Atomistic Simulation and Measurement of pH Dependent Cancer Therapeutic Interactions with Nanodiamond Carrier. *Mol. Pharmaceutics* **2011**, *8*, 368–374.
  28. Tisler, J.; Balasubramanian, G.; Naydenov, B.; Kolesov, R.; Grotz, B.; Reuter, R.; Boudou, J.-P.; Curmi, P. A.; Sennour, M.; Thorel, A.; et al. Fluorescence and Spin Properties of Defects in Single Digit Nanodiamonds. *ACS Nano* **2009**, *3*, 1959–1965.
  29. McGuinness, L. P.; Yan, Y.; Stacey, A.; Simpson, D. A.; Hall, L. T.; Maclaurin, D.; Prawer, S.; Mulvaney, P.; Wrachtrup, J.; Caruso, F.; et al. Quantum Measurement and Orientation Tracking of Fluorescent Nanodiamonds inside Living Cells. *Nat. Nanotechnol.* **2011**, *6*, 358–363.
  30. Liang, Y.; Ozawa, M.; Krueger, A. A General Procedure to Functionalize Agglomerating Nanoparticles Demonstrated on Nanodiamond. *ACS Nano* **2009**, *3*, 2288–2296.
  31. Heyer, S.; Janssen, W.; Turner, S.; Lu, Y.-G.; Yeap, W. S.; Verbeeck, J.; Haenen, K.; Krueger, A. Toward Deep Blue Nano Hope Diamonds: Heavily Boron-Doped Diamond Nanoparticles. *ACS Nano* **2014**, *8*, 5757–5764.
  32. Mohan, N.; Chen, C.-S.; Hsieh, H.-H.; Wu, Y.-C.; Chang, H.-C. *In Vivo* Imaging and Toxicity Assessments of Fluorescent Nanodiamonds in *Caenorhabditis Elegans*. *Nano Lett.* **2010**, *10*, 3692–3699.
  33. Hui, Y. Y.; Cheng, C.-L.; Chang, H.-C. Nanodiamonds for Optical Bioimaging. *J. Phys. D: Appl. Phys.* **2010**, *43*, 374021.
  34. Wu, T.-J.; Tzeng, V.-K.; Chang, W.-W.; Cheng, C.-A.; Kuo, Y.; Chien, C.-H.; Chang, H.-C.; Yu, J. Tracking the Engraftment and Regenerative Capabilities of Transplanted Lung Stem Cells Using Fluorescent Nanodiamonds. *Nat. Nanotechnol.* **2013**, *8*, 682–689.
  35. Hui, Y. Y.; Su, L.-J.; Chen, O. Y.; Chen, Y.-T.; Liu, T.-M.; Chang, H.-C. Wide-Field Imaging and Flow Cytometric Analysis of Cancer Cells in Blood by Fluorescent Nanodiamond Labeling and Time Gating. *Sci. Rep.* **2014**, *4*, 5574.
  36. Liu, K.-K.; Wang, C.-C.; Cheng, C.-L.; Chao, J.-I. Endocytic Carboxylated Nanodiamond for the Labeling and Tracking of Cell Division and Differentiation in Cancer and Stem Cells. *Biomaterials* **2009**, *30*, 4249–4259.
  37. Liu, K.-K.; Zheng, W.-W.; Wang, C.-C.; Chiu, Y.-C.; Cheng, C.-L.; Lo, Y.-S.; Chen, C.; Chao, J.-I. Covalent Linkage of Nanodiamond-Paclitaxel for Drug Delivery and Cancer Therapy. *Nanotechnology* **2010**, *21*, 315106.
  38. Perevedentseva, E.; Lin, Y.; Jani, M.; Cheng, C.-L. Biomedical Applications of Nanodiamonds in Imaging and Therapy. *Nanomedicine* **2013**, *8*, 2041–2060.
  39. Huang, H.; Pierstorff, E.; Osawa, E.; Ho, D. Active Nanodiamond Hydrogels for Chemotherapeutic Delivery. *Nano Lett.* **2007**, *7*, 3305–3314.
  40. Huang, H.; Pierstorff, E.; Osawa, E.; Ho, D. Protein-Mediated Assembly of Nanodiamond Hydrogels into a Biocompatible and Biofunctional Multilayer Nanofilm. *ACS Nano* **2008**, *2*, 203–212.
  41. Kumar, A.; Lin, P. A.; Xue, A.; Hao, B.; Yap, Y. K.; Sankaran, R. M. Formation of Nanodiamonds at Near-Ambient Conditions via Microplasma Dissociation of Ethanol Vapour. *Nat. Commun.* **2013**, *4*, 2618.
  42. Xing, Z.; Pedersen, T. P.; Wu, X.; Xue, Y.; Sun, Y.; Finne-Wistrand, A.; Kloss, F. R.; Waag, T.; Krueger, A.; Steinmüller-Nethl, D.; et al. Biological Effects of Functionalizing Copolymer Scaffolds with Nanodiamond Particles. *Tissue Eng., Part A* **2013**, *19*, 1783–1791.
  43. Havlik, J.; Petrakova, V.; Rehor, I.; Petrak, V.; Gulka, M.; Stursa, J.; Kucka, J.; Ralíš, J.; Rendler, T.; Lee, S.-Y.; et al. Boosting Nanodiamond Fluorescence: Towards Development of Brighter Probes. *Nanoscale* **2013**, *5*, 3208–3211.
  44. Mochalin, V. N.; Pentecost, A.; Li, X.-M.; Neitzel, I.; Nelson, M.; Wei, C.; He, T.; Guo, F.; Gogotsi, Y. Adsorption of Drugs on Nanodiamond: Toward Development of a Drug Delivery Platform. *Mol. Pharmaceutics* **2013**, *10*, 3728–3735.
  45. Mochalin, V. N.; Shenderova, O.; Ho, D.; Gogotsi, Y. The Properties and Applications of Nanodiamonds. *Nat. Nanotechnol.* **2011**, *7*, 11–23.
  46. Zhang, Q.; Mochalin, V. N.; Neitzel, I.; Knoke, I. Y.; Han, J.; Klug, C. A.; Zhou, J. G.; Leikes, P. I.; Gogotsi, Y. Fluorescent PLLA-Nanodiamond Composites for Bone Tissue Engineering. *Biomaterials* **2011**, *32*, 87–94.
  47. Wehling, J.; Dringen, R.; Zare, R. N.; Maas, M.; Rezwan, K. Bactericidal Activity of Partially Oxidized Nanodiamonds. *ACS Nano* **2014**, *8*, 6475–6483.
  48. Khanal, M.; Raks, V.; Issa, R.; Chernyshenko, V.; Barras, A.; Garcia Fernandez, J. M.; Mikhalovska, L. I.; Turchenik, V.; Zaitsev, V.; Boukherroub, R.; et al. Nanodiamonds: Selective Antimicrobial and Antibiofilm Disrupting Properties of Functionalized Diamond Nanoparticles Against *Escherichia Coli* and *Staphylococcus Aureus*. *Part. Part. Syst. Charact.* **2015**, *32*, 791–791.
  49. Ohara-Nemoto, Y.; Haraga, H.; Kimura, S.; Nemoto, T. K. Occurrence of *Staphylococci* in the Oral Cavities of Healthy Adults and Nasal-Oral Trafficking of the Bacteria. *J. Med. Microbiol.* **2008**, *57*, 95–99.
  50. Hancock, H. H. III; Sigurdsson, A.; Trope, M.; Moiseiwitsch, J. Bacteria Isolated after Unsuccessful Endodontic Treatment in a North American Population. *Oral Surg. Oral Med. Oral Pathol. Oral Radiol. Endod.* **2001**, *91*, 579–586.
  51. Wyman, T. P.; Dowden, W. E.; Langeland, K. *Staphylococcus Aureus* Isolation from a Clinically Nonexposed Root Canal. *J. Endod.* **1978**, *4*, 122–128.
  52. Fuda, C. C. S.; Fisher, J. F.; Mobashery, S.  $\beta$ -Lactam Resistance in *Staphylococcus Aureus*: The Adaptive Resistance of a Plastic Genome. *Cell. Mol. Life Sci.* **2005**, *62*, 2617–2633.
  53. Olajuyigbe, O. O.; Afolayan, A. J. Synergistic Interactions of Methanolic Extract of *Acacia Mearnsii* De Wild. with Antibiotics against Bacteria of Clinical Relevance. *Int. J. Mol. Sci.* **2012**, *13*, 8915–8932.
  54. Olajuyigbe, O. O. Synergistic Influence of Tetracycline on the Antibacterial Activities of Amoxicillin against Resistant Bacteria. *Journal of Pharmacy and Allied Health Sciences* **2012**, *2*, 12–20.
  55. Sujith, P. P.; Khendekar, V. D.; Girish, A. P.; Loka Bharathi, P. A. Immobilization of Nickel by Bacterial Isolates from the Indian Ridge System and the Chemical Nature of the Accumulated Metal. *Geomicrobiol. J.* **2010**, *27*, 424–434.
  56. Warnes, S. L.; Caves, V.; Keevil, C. W. Mechanism of Copper Surface Toxicity in *Escherichia Coli* O157:H7 and *Salmonella* Involves Immediate Membrane Depolarization Followed by Slower Rate of DNA Destruction which Differs from that Observed for Gram-Positive Bacteria. *Environ. Microbiol.* **2012**, *14*, 1730–1743.
  57. Cooper, G. M.; Le Couteur, D. G.; Richardson, D.; Buckley, N. A. A Randomized Clinical Trial of Activated Charcoal for the Routine Management of Oral Drug Overdose. *QJM* **2005**, *98*, 655–660.

58. Sadhasivam, S.; Chen, J.-C.; Savitha, S.; Hsu, M.-X.; Hsu, C.-K.; Lin, C.-P.; Lin, F.-H. Synthesis of Partial Stabilized Cement-Gypsum As New Dental Retrograde Filling Material. *Mater. Sci. Eng., C* **2012**, *32*, 1859–1867.
59. Wang, W.-H.; Lin, F.-H.; Lee, Y.-L.; Lin, C.-P. Cytotoxicity of Partial-Stabilized Cement. *J. Biomed. Mater. Res., Part A* **2007**, *81A*, 195–204.
60. Takushige, T.; Cruz, E. V.; Asfor Moral, A.; Hoshino, E. Endodontic Treatment of Primary Teeth Using a Combination of Antibacterial Drugs. *International Endodontic Journal* **2004**, *37*, 132–138.
61. Baer, J.; Maki, J. S. *In Vitro* Evaluation of the Antimicrobial Effect of Three Endodontic Sealers Mixed with Amoxicillin. *J. Endod.* **2010**, *36*, 1170–1173.
62. Baumgartner, J. C.; Xia, T. Antibiotic Susceptibility of Bacteria Associated with Endodontic Abscesses. *J. Endod.* **2003**, *29*, 44–47.
63. Marciano, J.; Michailescu, P. M. Dental Gutta-Percha: Chemical Composition, X-ray Identification, Enthalpic Studies, and Clinical Implications. *J. Endod.* **1989**, *15*, 149–153.
64. Möller, B.; Ørstavik, D. Chemical and Energy-Dispersive X-ray Analyses of Gutta-Percha Points. *J. Endod.* **1984**, *10*, 413–416.
65. Gurgel-Filho, E. D.; Andrade Feitosa, J. P.; Teixeira, F. B.; Monteiro de Paula, R. C.; Araújo Silva, J. B.; Souza-Filho, F. J. Chemical and X-ray Analyses of Five Brands of Dental Gutta-Percha Cone. *International Endodontic Journal* **2003**, *36*, 302–307.
66. Gencoglu, N.; Garip, Y.; Bas, M.; Samani, S. Comparison of Different Gutta-Percha Root Filling Techniques: Thermafil, Quick-Fil, System B, and Lateral Condensation. *Oral Surg. Oral Med. Oral Pathol. Oral Radiol. Endod.* **2002**, *93*, 333–336.